THE JOURNAL OF PHYSICAL CHEMISTRY C

pubs.acs.org/JPCC Article

Molecular-Level Understanding of Excited States of N-Annulated Rylene Dye for Dye-Sensitized Solar Cells

Changwon Kim, Tae Wu Kim, Siin Kim, Inhwan Oh, Henrike Wonneberger, Kihwan Yoon, Minseok Kwak, Joonghan Kim, Jeongho Kim, Chen Li, Klaus Müllen, and Hyotcherl Ihee*

Cite This: J. Phys. Chem. C 2020, 124, 22993−23003

ABSTRACT: In organic push−pull dyes for photovoltaics, it is important to understand the character of intramolecular charge transfer states. Accordingly, the dynamics of charge carriers in photosensitizers based on donor−acceptor structures have been widely studied. Recently, photosensitizers based on N-annulated rylene derivatives have been extensively utilized in organic solar cells due to their outstanding optical properties and considerable power conversion efficiencies, but the excited-state dynamics in those materials have not been investigated yet. Here, we explore the ultrafast dynamics of intramolecular charge transfer (ICT) occurring in the excited states of a diphenylamine N-annulated naphthalene dicarboximide derivative (DND) and present the photovoltaic performance of DND. By using steady-state absorption/emission spectroscopy, femtosecond broadband transient absorption spectroscopy, and DFT calculations, we found that the ICT dynamics of DND vary sensitively depending on the solvent polarity, and the ultrafast transition from the Franck−Condon state to the intramolecular charge transfer state is correlated to the solvation dynamics. This correlation underlines that the ultrafast ICT is strongly coupled with the solvation, accounting for the dependence of the ICT dynamics on the solvent polarity.

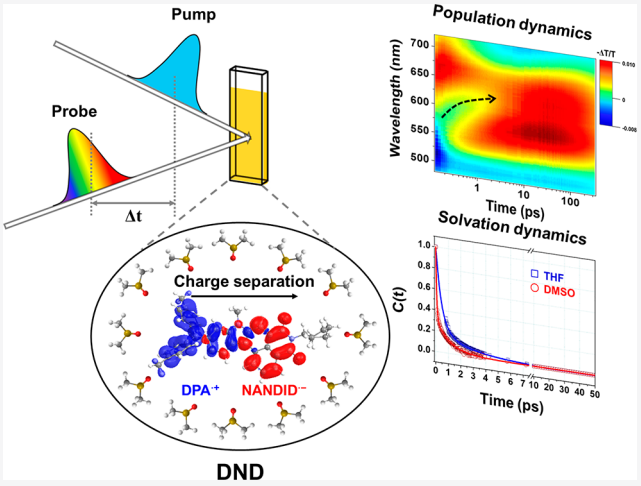

1. INTRODUCTION

Organic dyes play a crucial role as photosensitizers for nanoscale solar cells,[1,2] especially as an alternative for transition metal complexes that are toxic and of high cost. In particular, the photophysical properties of organic dyes can be fine-tuned by combining chemical moieties of different electron-donating or electron-withdrawing abilities[3−7] within a donor−acceptor (D−A) conjugation.[8−10] For so-called push−pull sensitizers employing D−A interaction, intramolecular charge transfer (ICT) occurs in their excited electronic states, thereby reducing the exciton binding energy and facilitating charge separation at the sensitizer/charge-acceptor interface.[11−13] To develop push−pull organic sensitizers optimized for highly efficient solar cells, one needs to understand the dynamic properties of the excited states of photosensitizers. Accordingly, many efforts have been dedicated to studying the dynamics of photogenerated carriers in various types of push−pull sensitizers.[11−21]

Rylene di- or tetracarboximides with aromatic cores made from naphthalene or peri-fused naphthalene moieties are versatile chromophores that can be utilized in nanoscale solar cells. Owing to their size expandability to perylene, terrylene, quaterrylene, and even higher homologues,[22,23] their optical properties can be widely varied.[23] The N-annulated derivatives containing a carbazole unit have received special attention.[24−36] This modification furnishes not only excellent optical properties, for example, high molar extinction coefficient and tunability of bandgap up to the near-IR region,[24,25] but also superb chemical properties such as stability, size expandability,[26] and exotic biradical characters.[27,28] Therefore, they are envisioned as promising building blocks of push−pull photosensitizers and have been used as electron donor[29−34] or π-linker[35] in push−pull sensitizers for solar cells[29−35] and photocatalysts.[33] For example, Luo and coworkers developed a dye-sensitized solar cell using an N-annulated perylene/Zn porphyrin hybrid dye with a power conversion efficiency (PCE) of up to ∼10.5%.[29] Despite the intense studies on the synthesis of N-annulated rylene-based photosensitizers and their photovoltaic characterization, the

Received: July 17, 2020
Revised: October 6, 2020
Published: October 14, 2020

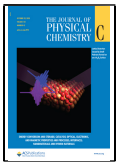

https://dx.doi.org/10.1021/acs.jpcc.0c06532
J. Phys. Chem. C 2020, 124, 22993−23003

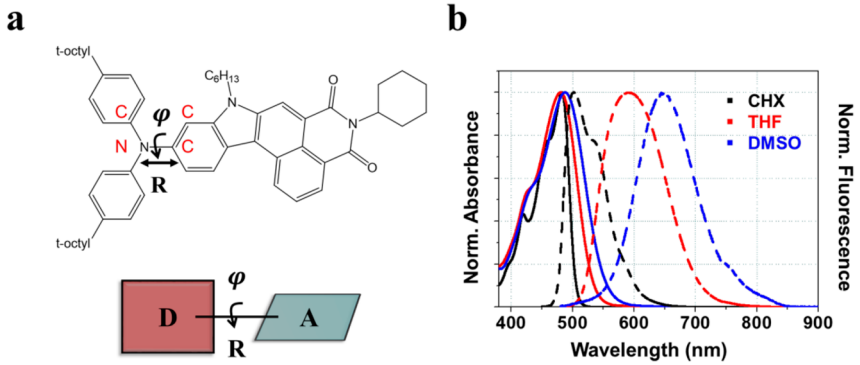

Figure 1. (a) Molecular structure of a diphenylamine-substituted N-annulated naphthalene dicarboximide derivative (DND). The dihedral angle, φ(C−C−N−C), and the bond length, R(C−N), between the main electron donor (DPA) and the electron acceptor (NANDID) moiety, which are indicated by a curved arrow and an arrow, are considered as key parameters in the relaxation of the excited states of DND. (b) Normalized steady-state absorption spectra (solid lines) and emission spectra (dashed lines) of DND in CHX (black), THF (red), and DMSO (blue). The emission spectra were measured with the excitation at 470 nm. It can be seen that the emission spectrum is spectrally red-shifted with the increase of solvent polarity.

carrier dynamics occurring in those rylene-based dyes have been rarely studied. Wang and co-workers have investigated the dynamics of electron injection from a related N-annulated perylene-based photosensitizer to TiO_2.[37,38] However, the dynamics of intramolecular charge transfer occurring on an ultrafast time scale in pristine N-annulated rylene-based photosensitizers have not been investigated yet.

In this work, we investigated the excited-state dynamics of a novel push−pull sensitizer, a diphenylamine N-annulated naphthalene dicarboximide derivative (DND), where diphenylamine (DPA) serves as the main electron donor and N-annulated naphthalene dicarboximide derivative (NANDID) as the electron acceptor, where the N-annulated part consists of an indole moiety linked to naphthalene (Figure 1a). Specifically, we investigated the early time dynamics of excited states, including ICT states and charge-separated (CS) states, on the subpicosecond to the picosecond time scale in DND using femtosecond broadband transient absorption (TA) spectroscopy. The femtosecond broadband TA measurement shows that the solvent polarity significantly influences the excited-state dynamics of DND and determines whether ICT or CS occurs. We also revealed that the charge carrier dynamics on an ultrafast time scale are strongly correlated to solvation dynamics. Furthermore, the quantum chemical calculations support that the excited-state relaxation leading to ICT is accompanied by structural changes. Finally, we fabricated a dye-sensitized solar cell (DSSC) using DND as a photosensitizer and characterized its photovoltaic performance.

2. EXPERIMENTAL METHODS

2.1. Materials. DND was synthesized for the spectroscopic measurement and the application to the organic photovoltaic devices. The details of the synthesis and characterization of DND are described in the Supporting Information. All chemicals and solvents were purchased from BASF or Sigma-Aldrich and used without further purification.

2.2. Steady-State Absorption and Steady-State/Time-Resolved Emission Spectroscopy. For the measurements of electronic absorption and fluorescence spectra, we used a UV/vis spectrophotometer (Shimadzu, UV-2550) and a fluorometer (PerkinElmer, LS-55), respectively. The fluorescence lifetime was measured with a time-correlated single-photon counting (TCSPC) technique (Edinburgh Instruments, FL920). The samples were excited with the 470 nm pulses from a diode laser, and the instrument response function of the TCSPC spectrometer was 270 ps. All sample solutions were placed into 1 mm thick quartz cells with nitrogen purging, and their optical densities (OD) were adjusted to be smaller than 0.2 at the excitation wavelength. For the measurement of the absolute fluorescence quantum yield (Φ_{fl}), we used an integrating sphere setup (Hamamatsu Photonics, Quantaurus-QY C13534-34).[39]

2.3. Broadband Transient Absorption Spectroscopy. Transient absorption spectra were measured with femtosecond laser pulses based on a visible pump−continuum probe scheme as described elsewhere.[40] The output pulses at the wavelength of 800 nm from a Ti:sapphire amplified laser (Coherent Legend Elite) were split into the pump and probe arms. On the pump arm, the 800 nm laser pulses were converted into the pump pulses with a wavelength of 473 nm and the bandwidth of 10 nm by using a home-built, all-reflective-optic noncollinear optical parametric amplifier. The pump pulses were sent through a pair of fused-silica prisms to precompensate for the dispersion obtained from transmissive optics and compressed to near-transform-limited pulses at the sample position. In the case of 400 nm excitation, the pump pulses with the wavelength of 400 nm and the bandwidth of 5 nm were generated by frequency-doubling using a 0.2 mm thickness β-barium borate (β-BBO) crystal and were not compressed further. At the sample position, the pulse energies of the pump pulses were adjusted to 150 nJ at 473 nm and 350 nJ at 400 nm. On the probe arm, the 800 nm laser pulses were sent into a c-cut sapphire window of 3 mm thickness and converted into a white light continuum spanning from visible to near-infrared wavelengths by self-phase modulation. The visible portion (480−720 nm) of the white light continuum was used as the supercontinuum probe without further compensation of the dispersion. The probe pulses were time-delayed with respect to the pump pulses by using a motorized translation stage (Newport, M-ILS150HA). The spectra of the transient absorption signal were detected by a spectrometer (Andor, SR303i) equipped with a CCD (Andor, DU420A). In all measurements, the polarization of the pump pulses was set to be a magic angle (54.7°) relative to that of the probe pulses. The time resolution of the transient absorption measurement was estimated as 47 fs from the optically heterodyne-detected

https://dx.doi.org/10.1021/acs.jpcc.0c06532
J. Phys. Chem. C 2020, 124, 22993−23003

Table 1. Photophysical Properties of DND in Various Solvents

solvent	ε_s[a]	λ_{abs}[b] (nm)	λ_{fl}[b] (nm)	τ_{fl}[c] (ns)	Φ_{fl}[d]	k_{nr}[e] ($\times 10^7$ s^{-1})	Stokes shift[f] (cm^{-1})
CHX	2.02	482.2	504.1	4.60	0.77	5.07	901
THF	7.58	480.1	598.7	6.20	0.55	7.30	4125
DMF	36.7	481.8	660.1				5605
MeCN	37.5	476.9	660.7				5834
DMSO	46.7	487.6	670.6	0.69	0.03	140	5595

[a]Static dielectric constants of solvent at 25 °C. [b]Wavelengths of absorption or emission maxima. [c]Obtained from TCSPC measurements. [d]Fluorescence quantum yields. [e]Rate constants of nonradiative relaxation. [f]The extent of the Stokes shift from absorption maxima to emission maxima in wavenumbers.

optical Kerr effect measurement of a pure solvent (CCl_4) at the sample position. All the sample solutions were deoxygenated by nitrogen gas purging before the measurements. The final solutions were placed in a 1 mm thick quartz cell, and the optical densities of solutions were adjusted to be 0.1−0.2 at the excitation wavelength.

2.4. Quantum Chemical Calculation. The molecular structures of the S_0 state of DND in the gas phase and solvent environment (cyclohexane (CHX), tetrahydrofuran (THF), and dimethyl sulfoxide (DMSO)) were optimized by using density functional theory (DFT). The PBE0, CAM-B3LYP, ωB97XD, MN12-SX, and MN15 functionals with 6-311++G(d,p) basis sets were employed in the DFT calculations. The solvent effects were considered by using the integral equation formalism polarizable continuum model (IEFPCM). The time-dependent DFT (TDDFT) method was used to calculate the vertical excitation energies (T_V's) of DND, and the results are summarized in Tables S1 and S2 of the Supporting Information. We carefully examined the basis set dependence on the T_V's and geometrical parameters via using other basis sets (6-31G(d,p) and 6-311G(d,p)), and the results are summarized in Tables S2 and S4. The calculated results in Tables S2 and S4 show that the basis set dependence is insignificant. The geometry optimizations of the S_1 states of DND were performed by using TDDFT with the same theoretical level of the DFT calculations to calculate emission energies of DND. The calculated results are also listed in Tables S1 and S3. All calculations were performed by using the Gaussian 16 package,[41] and the natural transition orbitals (NTOs) were visualized by using the Chemissian software.[42] Alkyl moieties were replaced by methyl groups for simplicity as this replacement was not likely to significantly alter the electronic structure of the target system.[43] The *XYZ* coordinates of the molecular structures in DMSO optimized by using the (TD-)MN15/6-311++G(d,p) are summarized in the Supporting Information.

2.5. Electrochemical Measurements. Cyclic voltammetry (CV) for spectroelectrochemistry experiments was performed by using a potentiostat (EG&G Princeton Applied Research, model 273). The working electrode consisted of a palladium−carbon electrode (1.5 mm diameter) that was polished on a felt pad with 0.05 μm alumina and washed with Milli-Q water before each experiment. A platinum wire was used as the counter electrode and an Ag wire as the reference electrode. The measurements were calibrated with ferrocene/ferrocenium (Fc/Fc^+). The CV measurements were performed in a solution of Bu_4NPF_6 (0.1 M) in dry dichloromethane with a scan rate of 50 mV s^{-1} at room temperature under argon. Conversion of energy on the absolute vacuum scale to the normal hydrogen electrode (NHE) was performed by using the relationship $E^0 = E_{abs} - 4.44$ V, where E^0 corresponds to the energy vs NHE and E_{abs} to the energy on the absolute vacuum scale.

2.6. Photovoltaic Fabrication and Performance Measurements. First, a TiO_2 blocking layer was prepared on an FTO-covered glass substrate by spray pyrolysis. Then, a TiO_2 paste (Dyesol) diluted with terpineol was applied by screen printing, resulting in a film thickness of 1.8 μm. All films were then sintered for 1 h at 450 °C and subjected to a 30 min treatment in a 40 mM aqueous solution of $TiCl_4$ at 65 °C, followed by another sintering step. The electrodes were then coated with dyes in a 0.5 mM dye solution in dichloromethane. The dye-coated TiO_2 electrodes contain an organic coadditive (BASF additives). Spiro-MeOTAD for a hole transporting material was applied by spin-coating from a solution in chlorobenzene containing 20 mM $Li(CF_3SO_2)_2N$. Device fabrication was completed by evaporation of 200 nm of silver as the counter electrode. The active area of the solid-state DSSCs was defined by the size of these contacts (0.13 cm^2), and the cells were masked with an aperture of the same area for measurements of cell performance. Current density−voltage ($I-V$) characteristics at 100 mW/cm^2 under AM 1.5G conditions and the external quantum efficiency (EQE) spectra were measured for all cells. The cells were assembled manually, however, in some steps by using apparatuses that allowed the treatment of several substrates at the same time, minimizing the error due to manual inaccuracies within one testing series. The titanium dioxide substrates, for example, were made in large batches by screen printing to achieve the same layer thickness for the substrates, and the back electrode was vapor-deposited on 10−16 substrates at the same time. To reduce measurement errors, two substrates of the same additive−solvent combination with four cells each were tested. The efficiencies presented here are an average of the cell results. Cells that did not reach 70% efficiency of the top cell among the eight cells were expected to have a major defect and were not included in the average. Still, cell results can vary. With the help of one standard dye, which has been included in all measurement series for several years now, the error of cell measurements could be estimated over the past years and is roughly ±0.2.

3. RESULTS AND DISCUSSION

3.1. Steady-State Absorption/Emission Spectra and Fluorescence Lifetime. To explore the effect of the solvent polarity on the photophysical properties of DND, steady-state absorption and emission spectra (Figure 1b and Figure S1) were measured for DND dissolved in various solvents such as cyclohexane (CHX), tetrahydrofuran (THF), *N*,*N*-dimethylformamide (DMF), acetonitrile (MeCN), and dimethyl sulfoxide (DMSO), which own dielectric constants of 2.02, 7.58, 36.7, 37.5, and 46.7, respectively. The absorption spectra

https://dx.doi.org/10.1021/acs.jpcc.0c06532
J. Phys. Chem. C 2020, 124, 22993−23003

of DND display a strong absorption around 480 nm and a weak absorption around 420 nm, common for all the solutions in various solvents, as shown in Figure S1. The emission spectra exhibit prominent emission in the visible region and, in CHX, are roughly the mirror images of the corresponding absorption spectra. In the nonpolar solvent of CHX, a vibronic feature with the energy splitting of 1070 cm^{-1} is observed in both absorption and emission spectra, whereas this feature becomes less pronounced in polar solvents of THF, DMF, MeCN, and DMSO. According to previous studies,[44,45] the energy splitting of 1070 cm^{-1} corresponds to the C=C stretching vibrations of aromatic rings of the perylene core. This splitting is not exactly the same as the 1400 cm^{-1} splitting observed in pristine perylene because the modification of the perylene core gives rise to perturbation in the electronic structure of the excited state. As the solvent polarity increases, the emission maximum is spectrally red-shifted, while the maximum of the lowest absorption band reveals negligible solvent dependence (Table 1). Such a bathochromic spectral shift can be quantified by the Lippert−Mataga equation (Figure S2):

$$\tilde{\nu} = \tilde{\nu}_{abs} - \tilde{\nu}_{fl} = \frac{2\Delta f}{hca_0^3}(\Delta\vec{\mu}_{eg})^2 + \text{const} \quad (1)$$

$$\Delta f = \frac{\varepsilon_s - 1}{2\varepsilon_s + 1} - \frac{n^2 - 1}{2n^2 + 1} \quad (2)$$

where $\tilde{\nu}_{abs}$ and $\tilde{\nu}_{fl}$ represent the maxima of absorption and emission spectra in the unit of wavenumber, ε_s is the static dielectric constant of solvents at 25 °C, and n is the refractive index of solvents at 20 °C. $\Delta\vec{\mu}_{eg}$ represents the dipole moment change between the excited state ($\vec{\mu}_e$) and the ground state ($\vec{\mu}_g$), c is the speed of light, h is Planck's constant, and a_0 is the radius of the chromophore molecule determined based on Onsager's model. According to the analysis using the Lippert−Mataga equation, the spectral Stokes shift ($\Delta\tilde{\nu}$) and the orientation polarizability (Δf) indicate a distinct linear correlation. From the slope of 16730 cm^{-1} in the Lippert−Mataga plot, $\Delta\vec{\mu}_{eg}$ is estimated to be 21.1 D.

The fluorescence lifetimes of DND measured in various solvents of different polarities are presented in Figure S3 and Table 1. It can be seen that the increase of solvent polarity induces the decrease of both fluorescence quantum yield (Φ_{fl}) and fluorescence lifetime (τ_{fl}) and thus the increase of the rate constant of nonradiative relaxation (k_{nr}) according to eq S2; the values of k_{nr} in CHX, THF, and DMSO are 5.07×10^7, 7.30×10^7, and 1.40×10^9 s^{-1}, respectively. Considering the spectral red-shift of the emission maximum with the increase of solvent polarity, we can infer that the nonradiative relaxation from the excited state to the ground state is accelerated with the decrease of the energy gap between the lowest excited state and the ground state, as expected from the energy-gap law.[46,47] This emission behavior deduced from fluorescence measurements is in accord with ICT observed in other D−A conjugated dyes.[48−54]

3.2. Quantum Chemical Calculations. To gain insight into the electronic structure of DND, we conducted quantum chemical calculations. For the comparison with experimental absorption and emission spectra, we performed the TDDFT calculations using PBE0, CAM-B3LYP, ωB97XD, MN12-SX, and MN15/6-311++G(d,p) levels of theory with the IEFPCM method to consider the solvent effect (Table S1). According to the calculated results, the lowest optical transition from $S_0 \rightarrow S_1$ is dominated by the HOMO−LUMO transition (at least 85%) in all calculations except the MN12-SX calculation for the gas phase. As can be seen from Table S1, PBE0 and MN12-SX underestimate the vertical excitation energies (T_V's) of DND in the three different solvents. In contrast, CAM-B3LYP, ωB97XD, and MN15 overestimate the T_V's of DND, but the results of MN15 are the closest to the experimental values. In the case of emission, both PBE0 and MN12-SX underestimate the emission energies in the CHX and THF solvent. In contrast, CAM-B3LYP, ωB97XD, and MN15 overestimate the emission energies in all three solvents. Among them, MN15 gives the closest results to the experimental values; especially, the emission energy in CHX calculated by MN15 is in excellent agreement with the experiment (Table S1). Although CAM-B3LYP overestimates the T_V's of DND, a recent study has shown that CAM-B3LYP correctly describes the charge transfer (CT) characteristics.[55] Because MN15 provides the most reasonable results, in particular, the dipole moments (Table S5) that show the same trend as CAM-B3LYP, we expected that MN15 should describe the CT characteristics well and is the most appropriate functional for calculating the excitation properties of DND. For this reason, hereafter, we use the geometrical parameters and the T_V's calculated with the MN15 functional for most discussions. Furthermore, we performed DFT and TDDFT calculations using five functionals (PBE0, CAM-B3LYP, ωB97XD, MN12-SX, and MN15) with 6-31G(d,p) and 6-311G(d,p) to examine the basis set dependence on the T_V calculations. As can be seen from Table S2, the basis set dependencies in the DFT and TDDFT calculations are insignificant. Thus, hereafter, we analyzed only the results of MN15/6-311++G(d,p) for further discussion. To clearly demonstrate the charge distribution in DND, we represented the natural transition orbitals (NTOs),[56] which reveal the combination of single particle−hole transitions corresponding to the electronic absorption and can be used as an intuitive means of describing the origin of the transition. For the lowest electronic transition, the charge density of the particle in NTOs is predominantly localized at the NANDID acceptor moiety, and the charge density of the hole in NTOs is delocalized over the DPA and the N-annulated linker-like moiety (see Figure 2c,d). As shown in Figure 2e, the difference between the calculated charge densities of hole and particle for the lowest electronic transition clearly exhibits the separation of charge densities between donor and acceptor moieties, supporting the occurrence of intramolecular CT in DND. The details of the comparison among the calculations with various functionals and basis sets are summarized in the Tables S1−S5.

In accordance with the ICT behavior identified in the NTO picture, the $S_0 \rightarrow S_1$ transition accompanies the dramatic change in the magnitude of the dipole moment of DND. According to the (TD-)MN15 calculations, the dipole moment of DND is 8.7 D in the ground state and increases up to 27.7 D in the first singlet excited state in DMSO solvent, as presented in Table S5, giving the vector difference of the dipole moment, $\Delta\vec{\mu}_{eg}$, of 19.0 D. The $\Delta\vec{\mu}_{eg}$ value of 19.0 D calculated by (TD-)MN15 agrees well with the experimental value (21.1 D) estimated from the Lippert−Mataga plot of the absorption and emission maxima (Figure S2). Such a large vector difference of the dipole moments between the ground and the singlet excited states highlights the strong ICT character of the singlet excited state of the DND. On the basis of the TDDFT

https://dx.doi.org/10.1021/acs.jpcc.0c06532
J. Phys. Chem. C 2020, 124, 22993−23003

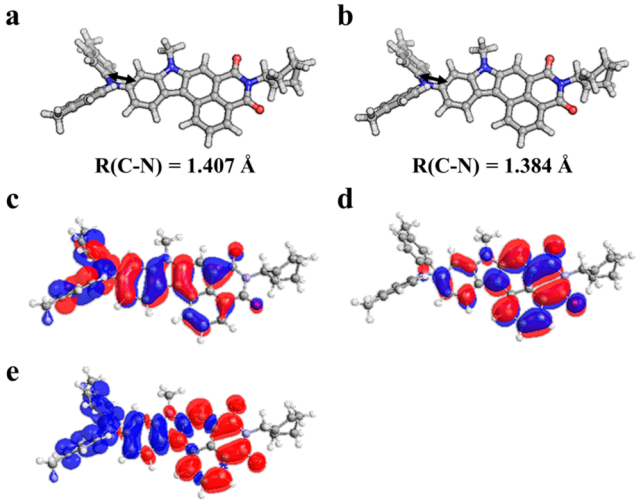

Figure 2. (a, b) Molecular structure of DND optimized with (TD)DFT/MN15/6-311++G(d,p) by using the IEFPCM (DMSO solvent) for (a) the ground state and (b) the singlet excited state (S_1/ICT). The bond length, R(C−N), between DPA and NANDID moieties is indicated by a black arrow. (c, d) Charge densities of (c) hole and (d) particle for the lowest transition represented in terms of NTO. (e) Difference between the charge densities of hole and particle for the lowest transition. The electron-rich (red) and the electron-deficient (blue) regions are spatially separated, supporting the occurrence of intramolecular charge transfer in DND.

calculations, the lowest electronic transition can be regarded as the ICT transition from the donor to the acceptor moiety.

3.3. Broadband Transient Absorption Spectra. To explore the dynamics of intramolecular charge transfer in DND and their solvent dependence, we performed femtosecond broadband TA measurements for DND dissolved in three different solvents: CHX, THF, and DMSO. The laser pulse at 473 nm center wavelength with the bandwidth of 10 nm full width at half-maximum (FWHM) was used to excite the samples. Figure 3 gives the broadband TA spectra of DND in the three solvents. To extract the time-dependent change of the TA signals, we performed a global fitting analysis of the broadband TA data based on sequential kinetics. As shown in Figure 3, the spectral features of each intermediate are represented as species-associated difference spectra (SADS), each of which corresponds to a spectrum characteristic of an intermediate species involved in the relaxation of excited states. The kinetics for the transitions among the SADS are represented by time constants listed in Table 2.

According to the global analysis of the TA data for DND in CHX (Figure 3a,b), the first SADS displays prominent stimulated emission (SE) at 480−550 nm with peaks at 492 and 532 nm and broad excited-state absorption (ESA) at 550−720 nm. With subsequent transitions from the first SADS to the third SADS, the SE band is red-shifted gradually, giving the peaks at 500 and 538 nm in the third SADS. These SE peaks correspond to the peaks of vibronic progression (504 and 537 nm) observed in the steady-state fluorescence spectrum (Figure S5). The spectral red-shift of the SE band without any significant change of spectral shape indicates that photoexcited DND in CHX undergoes only vibrational cooling without any transition to another electronic state.

In contrast, the TA spectra of DND in polar solvents, THF and DMSO, exhibit markedly different spectral features compared with those in CHX, indicating that the excited states of DND in the polar solvents undergo relaxation through different electronic states from the DND in the nonpolar CHX solvent. For DND in THF (Figure 3c,d), the first SADS exhibits the GSB and SE features at 480−560 nm with a peak at 520 nm. By the transition from the first SADS to the second SADS with the time constant of τ_1 = 427 fs, the SE feature around 520 nm is red-shifted and quenched while the ESA feature at 510−570 nm simultaneously grows up. Subsequent transitions from the second SADS occur with time constants of τ_2 = 1.35 ps (to the third SADS) and τ_3 = 8.14 ps (to the fourth SADS) while being accompanied by a spectral red-shift and the quenching of the SE feature as well as further growth of the ESA feature at 510−570 nm (Figure 3d).

For DND in DMSO (Figure 3e,f), the TA spectra change in a similar manner to those in THF, with the significant quenching of SE around 525 nm and the growth of ESA at 510−600 nm. However, the transition from the first SADS to the second SADS is faster in DMSO (τ_1 = 195 fs time constant) than in THF (τ_1 = 427 fs time constant), and the growth of ESA feature around 545 nm in the second SADS is more significant than in THF. In the third SADS and fourth SADS, the SE feature is quenched more significantly, and the ESA feature further grows up in a much broader spectral range of 510−610 nm (Figure 3f) than in the third SADS and fourth SADS in THF, and these transitions occur more slowly (τ_2 = 1.51 ps to the third SADS and τ_3 = 11.8 ps to the fourth SADS) than those in THF. Such different temporal changes of the TA spectra in DMSO and THF after second SADS suggest that the relaxation pathways of excited states of DND in the two solvents are quite different from each other, especially on the picosecond time scale.

The temporal changes of TA spectra suggest that the solvent polarity affects the formation of the ICT state. For DND in polar solvents (THF and DMSO), the earliest transition from the first SADS to the second SADS accompanies the growth of ESA at 510−600 nm. This transition can be attributed to the formation of the S_1/ICT state as a similar ESA feature at 500−600 nm has been identified as a signature of an ICT state in previous studies on perylene *N*,*N*-dimethylaniline (PeDMA)[48] and tetrahydro[5]helicene-based imide triphenylamine (THHBI-PhNPh$_2$).[50] In addition to the change of ESA, in polar solvents, the SE feature at 500−560 nm in the first SADS is significantly red-shifted in the second SADS, with the peak at 570 nm in THF and at 600 nm in DMSO. These two spectrally distinct SE characteristics observed in the first and second SADS correspond to dual emission from FC and ICT states, which is commonly observed in the D−A molecules as the evidence of ICT transition.[52,57] Thus, the first and second SADS can be assigned to the S_1/FC state and the S_1/ICT state, respectively.

Also, it should be noted that the growth of the ESA feature at 550−650 nm with the transitions from the second SADS to the third and fourth SADS is more significant in DMSO than in THF (Figure S6), suggesting that the ICT state in DMSO relaxes via different states compared with that in THF. This ESA feature can be assigned to the radical anion of NANDID (NANDID$^{\bullet-}$) because a similar feature was observed in the transient absorption spectra of naphthalene tetracarboxdiimide derivatives mixed with a strong electron donor and assigned as the signature of a radical anion species.[58] The NANDID$^{\bullet-}$ species is formed by the transfer of one full quantum of an electron from DPA to NANDID, that is, the formation of the charge-separated (CS) state. Because fluorescence would be

https://dx.doi.org/10.1021/acs.jpcc.0c06532
J. Phys. Chem. C 2020, 124, 22993−23003

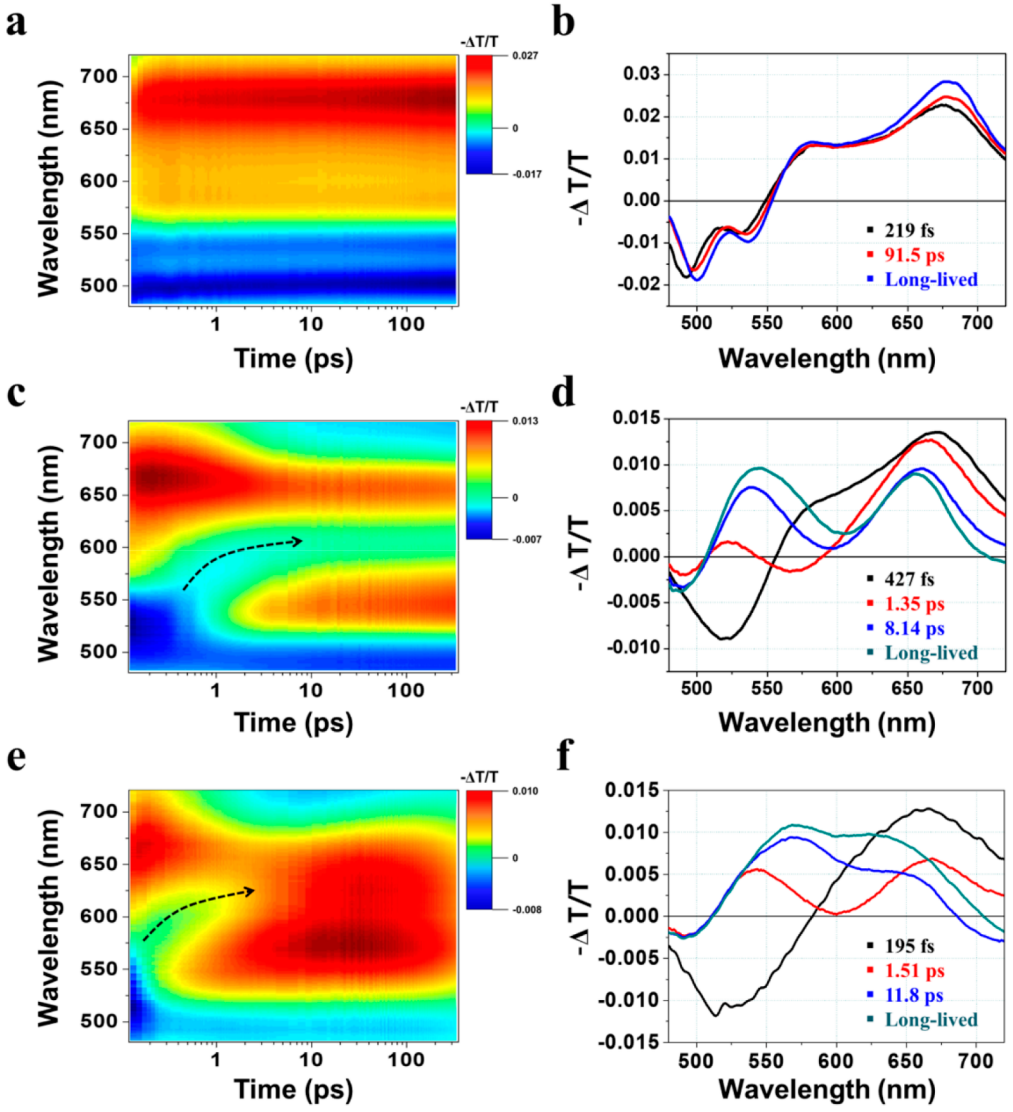

Figure 3. (a) Two-dimensional TA spectra and (b) SADS of DND in CHX. (c) Two-dimensional TA spectra and (d) SADS of DND in THF. (e) Two-dimensional TA spectra and (f) SADS of DND in DMSO after excitation at 473 nm. The SADSs are obtained from the global analysis of TA data based on the sequential kinetics. The time constant corresponding to the relaxation of each SADS is indicated. The black dashed arrows in (c) and (e) indicate the spectral red-shift of SE bands.

Table 2. Time Constants Determined from TA Measurements and the Solvation Time Correlation Function, $C(t)$

	TA				$C(t)$	
solvent	τ_1 (fs)	τ_2 (ps)[a]	τ_3 (ps)	τ_4 (ns)[a]	τ_1 (fs)	τ_2 (ps)
CHX	219 ± 41	91.5 ± 20.6		4.6		
THF	427 ± 11	1.35 ± 0.04	8.14 ± 0.46	6.2	448 ± 9	2.40 ± 0.08
DMSO	195 ± 5	1.51 ± 0.04	11.8 ± 0.3	0.69	71 ± 3	1.07 ± 0.02

[a]Time constants were fixed at the values determined from time-resolved fluorescence measurements using TCSPC.

quenched by charge separation, the exceptionally small Φ_{fl} in DMSO is consistent with the formation of CS state. In agreement with our result, in a previous study of an N-annulated perylene tetracarboxdiimide dimer,[59] it was reported that the thermodynamic stability of the CS state is governed by solvent polarity, and thus the CS state is formed only in highly polar solvents.

3.4. Structural Change Induced by ICT. Many studies[50,53,54,57,60,61] on push−pull dyes concluded that ICT is accompanied by structural changes. For example, on the basis of DFT calculations, it has been suggested that the lowest singlet excited state (that is, the ICT state) of D−A or D−A−D dyes possess twisted geometries, with larger[53,54] or smaller[50,60] donor−acceptor dihedral angles than the ground state. Also, it was suggested that the transition from an ICT state with planar geometry to an ICT state with twisted geometry goes along with an increase of the dipole moment.[57,61]

To examine the structural change occurring in the excited states of DND, we performed TD-MN15/6-311++G(d,p)

https://dx.doi.org/10.1021/acs.jpcc.0c06532
J. Phys. Chem. C 2020, 124, 22993−23003

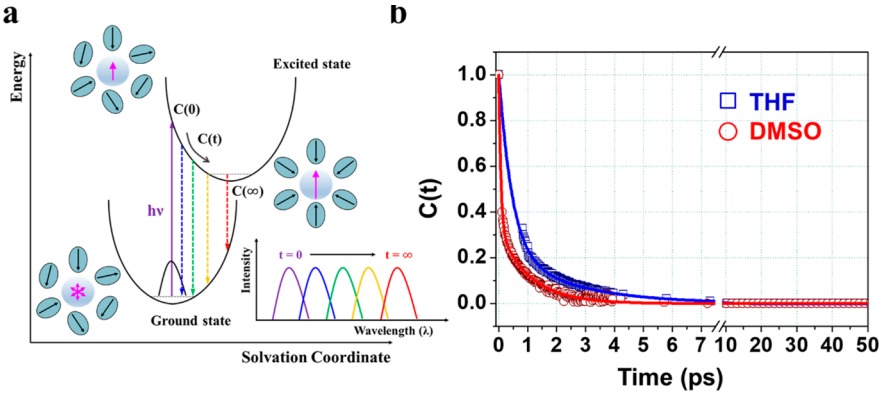

Figure 4. (a) Upon electronic excitation of the solute, the dipole moment of a solute molecule is transiently aligned along the direction of laser polarization. Subsequently, solvent molecules in the solvation cage are reoriented following the excited-state orientation of the solute dipole moment. This solvation process involves a spectral red-shift of the stimulated emission and can be quantitatively described by a solvation time correlation function, $C(t)$. The dipole moment of the solute is indicated with a magenta arrow, whose length indicates its relative magnitude. (b) Solvation time correlation function, $C(t)$, obtained from the TA spectra of DND in THF (blue squares) and DMSO (red circles). The $C(t)$'s were fitted by the sum of two exponentials (solid lines), and their time constants are listed in Table 2.

calculations with the IEFPCM method (Table S3). It is readily expected that the transition to the S_1/ICT state will accompany the shortening of R(C−N) because the hole of NTO has an antibonding character (Figure 2c) and the particle of NTO has a nonbonding character. Indeed, as can be seen from Figure 2a,b, the R(C−N) of DND in DMSO decreases from 1.407 to 1.384 Å (δR(C−N) = 0.023 Å). The rotation along the φ(C−C−N−C) angle of DND is inherently hindered due to the increased steric hindrance[62] by the strengthening of the C−N bond. The DND differs from other systems where a change of the dihedral angle is accompanied by the intramolecular CT state, resulting in the twisted ICT (TICT) state. We identified that the ICT character increases as the solvent polarity increases via the difference dipole moment vector (Table S5). This result can also be identified in terms of the magnitude of the shortening of R(C−N). As the solvent polarity increases, the degree of shortening of R(C−N) also increases (δR(C−N) = 0.005 (gas phase), 0.012 (CHX), 0.019 (THF), and 0.023 Å (DMSO)). In the case of DND, the R(C−N) bond is an indicator of the magnitude of ICT character like a dihedral angle of TICT. That is, the extent of the structural rearrangement in DMSO is the largest among three solvents, and this is consistent with the tendencies of the Stokes shift of emission energies as the solvent polarity increases (Table 1 and Table S1).

3.5. Intramolecular Charge Transfer Coupled with Solvation. We have assigned the early time dynamics of SE quenching and ESA growth in the TA spectra, which are observed only for DND in polar solvents, to the formation of ICT state. Considering that the polarity of solvent governs the formation of ICT state, we can infer that the intramolecular charge transfer in DND is associated with the solvation.[50] As a means of verifying this hypothesis, the time-dependent fluorescence Stokes shift[63] can be used. The temporal change of the Stokes shift of the fluorescence spectrum of a polar solute molecule can serve as a measure of the solvation dynamics (see Figure 4a). Because the SE feature of the TA spectra is equivalent to fluorescence, the solvation dynamics can be extracted from the SE dynamics of the TA spectra. In particular, we have extracted the solvation time correlation function (or spectral response function), $C(t)$, from the SE bands in the TA spectra for DND in each solvent using the following equation:[63−66]

$$C(t) = \frac{\nu(t) - \nu(\infty)}{\nu(0) - \nu(\infty)} \tag{3}$$

where $\nu(t)$ represents the frequency of the SE peak at each time delay, $\nu(\infty)$ stands for the frequency of the emission peak of the steady-state emission spectrum, and $\nu(0)$ is the peak position of SE band at time zero. However, since the TA spectrum around the zero delay time can be contaminated by nonresonant electronic response arising from the interaction of pump and probe pulses, the value of the peak position at time-zero for polar solvent ($\nu_p(t = 0)$) was calculated via the following equation:[67]

$$\nu_p(t = 0) \approx \nu_p(\text{abs}) - [\nu_{np}(\text{abs}) - \nu_{np}(\text{em})] \tag{4}$$

where ν_{np}(abs) and ν_{np}(em) are the peak positions of the steady-state absorption and emission spectra in a nonpolar solvent (CHX), respectively, and ν_p(abs) represents the peak position of the steady-state absorption spectrum in polar solvents (THF or DMSO). At each time delay, the peak position of the SE band was determined from the fitting of a corresponding TA spectrum with multiple Gaussian functions as presented in Figure S8, and the determined frequency was then used for the calculation of the solvation time correlation function, $C(t)$. The temporal traces of $C(t)$ for THF and DMSO are shown in Figure 4b. By fitting $C(t)$ with multiple exponentials, we determined the time constants of 448 fs and 2.40 ps for THF and 71 fs and 1.07 ps for DMSO, as listed in Table 2. The decay rates of $C(t)$ obtained from our data are close to the solvation rates observed in the previous studies on solvation dynamics of THF and DMSO.[64,65]

The decay times of $C(t)$ are in good agreement with the two earliest transition times of DND determined from the analysis of TA spectra. The first solvation time is assigned to the inertial motion of solvent molecules and is similar to the transition time from the first SADS to second SADS (τ_1), that is, the formation time of S_1/ICT. The similarity of these two time constants indicates the correlation between the solvation dynamics and the ICT formation dynamics, implying that the solvent cage serves as a driving force for the S_1/FC → S_1/ICT

https://dx.doi.org/10.1021/acs.jpcc.0c06532
J. Phys. Chem. C 2020, 124, 22993−23003

transition in polar solvents.[48] The slower component of the solvation dynamics is assigned to the diffusive reorientation of solvent molecules and matches the time scale of the transition from the second SADS to third SADS (τ_2). As the transition from the second SADS to third SADS corresponds to the vibrational relaxation of the ICT state, it is probable that the energy dissipation to vibrational modes of solvent molecules mediates the vibrational relaxation. The agreement in the time scales of the excited-state relaxation of DND and the solvation implies that the formation of the ICT state is strongly coupled with solvent reorganization.[51,61,68] There have been studies[50,51,60,68−72] showing that the formation or relaxation of the ICT state is strongly correlated to solvation. For example, in TA studies on D−A dyads[50,69−72] or D−π−A−π−D triads,[60] the dynamics of the ICT formation and relaxation are on the same time scale as $C(t)$ extracted from the SE features in the TA spectra. Also, time-resolved fluorescence measurements have revealed a correlation between the ICT dynamics and solvation dynamics in D−A dyads.[51,68] We note that for DND the solvation is much faster and comes with a larger Stokes shift in DMSO than in THF (Figure S9). The accelerated solvation dynamics in DMSO is in agreement with the faster formation of ICT state in DMSO, as evidenced by faster growth of ESA at ∼550 nm in the transition from the first SADS to the second SADS in the TA spectra (Figure 3c,e).

3.6. Excited-State Dynamics of DND. On the basis of the transient absorption spectra and their kinetic analysis, we propose the excited-state dynamics of DND in CHX, THF, and DMSO schematically described in Figure 5. In CHX (Figure 5a), the S_1/FC state is initially populated by photoexcitation, and vibrational relaxation in the S_1/FC state occurs with the time constant of τ_1 = 219 fs. Subsequently, the relaxation of the S_1/FC state takes place with the time constant of τ_2 = 91.5 ps. Because the spectral shape of the TA spectrum changes only mildly by this process, this transition may involve structural changes, rather than formation of an ICT state, which is known to induce a significant change of the TA spectrum. The lack of an ICT state for DND in CHX can be attributed to the nonpolar character of CHX, where the ICT (or CS) state with spatial charge separation would not be stable. In contrast, in THF (Figure 5b), the initially excited S_1/FC state relaxes to the ICT state with the τ_1 = 427 fs time constant.[57,61] Then, the vibrational relaxation of the ICT state occurs with the time constant of τ_2 = 1.35 ps. On the basis of the similar time scales of the ICT relaxation and the solvation dynamics described by $C(t)$, it can be concluded that the ultrafast dynamics of the ICT relaxation is strongly coupled with the solvation dynamics in THF.[64] The ICT state undergoes further transition with the time constant of τ_3 = 8.14 ps. According to the DFT calculations (section 3.4), the formation of the ICT state accompanies the shortening of the C−N bond. On the basis of this result, the state intermediate formed by the transition of the initially generated ICT state can be assigned to another ICT state with a shortened C−N bond, which eventually relaxes to the ground state. In DMSO (Figure 5c), the S_1/FC → S_1/ICT transition occurs with the time constant of τ_1 = 195 fs. Subsequently, the CS state is generated from the ICT state with the time constant of τ_2 = 1.51 ps. Because the CS state is stabilized in the highly polar environment of DMSO, the transition to the CS state is thermodynamically favorable in DMSO.[59] Both of the two earliest transitions of photoexcited DND in DMSO are coupled with the solvation, as in THF. Then, the CS state

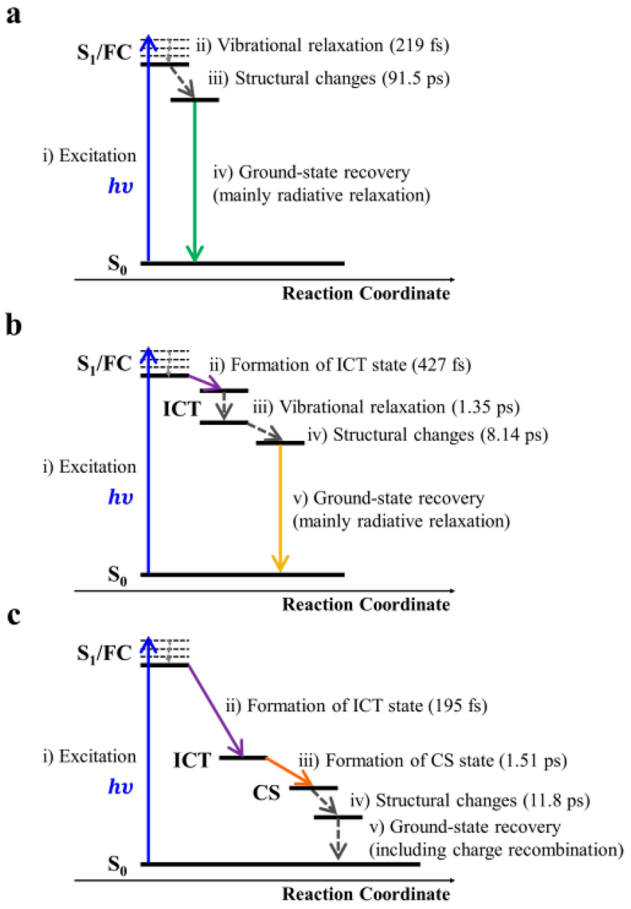

Figure 5. Excited-state dynamics of DND in (a) CHX, (b) THF, and (c) DMSO. In CHX, considering the monotonic spectral change of TA spectra, only the vibrational relaxation and the structural changes occur in the excited states. However, in polar solvents of THF and DMSO, the ICT states are formed exhibiting significant quenching and red-shift of SE in TA spectra. In DMSO, the CS state is formed from the ICT state because the CS state is stable in the highly polar environment of DMSO.

undergoes structural changes with the time constant of τ_3 = 11.8 ps. It should be noted that the structural rearrangement (the transition from third SADS to fourth SADS in the TA spectra) is slower in DMSO than in THF, which can be explained by the viscosities of DMSO (η = 2.00) and THF (η = 0.46).[73,74] Finally, the ground state is nonradiatively recovered from the structurally changed CS state by charge recombination.

4. CONCLUSION

In the present work, we described the ultrafast ICT dynamics of a novel DND dye using steady-state optical spectroscopy, femtosecond broadband transient absorption spectroscopy, and quantum chemical calculations and presented the photovoltaic performance of DND in a DSSC device. Although the sensitizer is typically used in the solid device, we examined the effect of the solvent polarity on the excited-state dynamics to understand how the dynamics of DND is influenced by the environment. In particular, the excited-state dynamics of DND in various solvents were monitored by TA spectra, and a series of excited states involved in the relaxation from the initially excited state were characterized. Most importantly, we found

https://dx.doi.org/10.1021/acs.jpcc.0c06532
J. Phys. Chem. C 2020, 124, 22993−23003

that the solvent polarity affects the excited-state dynamics of DND significantly and even determines whether an ICT or a CS state is formed. The relatively low PCE of the DND-based solar cell tested in this work (see Supplementary Note 5, Table S6, and Figure S10 in the Supporting Information) can be attributed to the large bandgap of DND, which cannot absorb light in the entire visible and near-IR region of the sunlight. Nevertheless, rylene derivatives have an excellent size tunability toward larger rylene units such as perylene, terrylene, quaterrylene, and even higher homologues,[75] and thus it would be feasible to develop a rylene compound that can absorb in a broader spectral range up to the near-IR region. With the rylene derivative with a smaller bandgap, the solar cells with higher efficiencies would be achievable. The excited-state dynamics associated with the solvent polarity determined in this work would provide a guideline for utilizing the N-annulated rylene-based sensitizers in photovoltaic applications.

■ ASSOCIATED CONTENT

Supporting Information

The Supporting Information is available free of charge at https://pubs.acs.org/doi/10.1021/acs.jpcc.0c06532.

Details on synthesis and characterization results of DND; steady-state spectroscopy results and TCSPC data; additional DFT and TDDFT results; kinetic analysis of TA data; photovoltaic data of DND-1; Cartesian coordinates for optimized geometries of DND (PDF)

■ AUTHOR INFORMATION

Corresponding Author

Hyotcherl Ihee − *Department of Chemistry and KI for the BioCentury, Korea Advanced Institute of Science and Technology (KAIST), Daejeon 34141, Republic of Korea; Center for Nanomaterials and Chemical Reactions, Institute for Basic Science (IBS), Daejeon 34141, Republic of Korea;* orcid.org/0000-0003-0397-5965; Phone: +82-42-350-2844; Email: hyotcherl.ihee@kaist.ac.kr

Authors

Changwon Kim − *Department of Chemistry and KI for the BioCentury, Korea Advanced Institute of Science and Technology (KAIST), Daejeon 34141, Republic of Korea; Center for Nanomaterials and Chemical Reactions, Institute for Basic Science (IBS), Daejeon 34141, Republic of Korea*

Tae Wu Kim − *Center for Nanomaterials and Chemical Reactions, Institute for Basic Science (IBS), Daejeon 34141, Republic of Korea;* orcid.org/0000-0002-6370-0907

Siin Kim − *Department of Chemistry and KI for the BioCentury, Korea Advanced Institute of Science and Technology (KAIST), Daejeon 34141, Republic of Korea; Center for Nanomaterials and Chemical Reactions, Institute for Basic Science (IBS), Daejeon 34141, Republic of Korea*

Inhwan Oh − *Department of Chemistry and KI for the BioCentury, Korea Advanced Institute of Science and Technology (KAIST), Daejeon 34141, Republic of Korea; Center for Nanomaterials and Chemical Reactions, Institute for Basic Science (IBS), Daejeon 34141, Republic of Korea*

Henrike Wonneberger − *BASF SE, Ludwigshafen 67056, Germany*

Kihwan Yoon − *Department of Chemistry, The Catholic University of Korea, Bucheon 14662, Republic of Korea*

Minseok Kwak − *Department of Chemistry, Pukyong National University, Busan 48513, Republic of Korea;* orcid.org/0000-0002-0480-1804

Joonghan Kim − *Department of Chemistry, The Catholic University of Korea, Bucheon 14662, Republic of Korea;* orcid.org/0000-0002-7783-0200

Jeongho Kim − *Department of Chemistry, Inha University, Incheon 22212, Republic of Korea;* orcid.org/0000-0003-4085-293X

Chen Li − *School of Environment and Civil Engineering, Dongguan University of Technology, Dongguan, Guangdong Province, P. R. China;* orcid.org/0000-0002-8438-259X

Klaus Müllen − *Max Planck Institute for Polymer Research, 55128 Mainz, Germany*

Complete contact information is available at: https://pubs.acs.org/10.1021/acs.jpcc.0c06532

Notes

The authors declare no competing financial interest.

■ ACKNOWLEDGMENTS

This work was supported by the Institute for Basic Science (IBS-R004). This work was also supported by the Basic Science Research Program through the National Research Foundation of Korea (NRF) funded by the Ministry of Science, ICT & Future Planning (NRF-2016R1E1A1A01941978).

■ REFERENCES

(1) Mishra, A.; Fischer, M. K.; Bäuerle, P. Metal-free organic dyes for dye-sensitized solar cells: from structure: property relationships to design rules. *Angew. Chem., Int. Ed.* **2009**, *48*, 2474−99.

(2) Li, G.; Zhu, R.; Yang, Y. Polymer solar cells. *Nat. Photonics* **2012**, *6*, 153−161.

(3) Kim, B. G.; Chung, K.; Kim, J. Molecular design principle of all-organic dyes for dye-sensitized solar cells. *Chem. - Eur. J.* **2013**, *19* (17), 5220−5230.

(4) Teng, C.; Yang, X.; Li, S.; Cheng, M.; Hagfeldt, A.; Wu, L. Z.; Sun, L. Tuning the HOMO energy levels of organic dyes for dye-sensitized solar cells based on Br−/Br3− electrolytes. *Chem. - Eur. J.* **2010**, *16* (44), 13127−13138.

(5) Gao, P.; Tsao, H. N.; Grätzel, M.; Nazeeruddin, M. K. Fine-tuning the electronic structure of organic dyes for dye-sensitized solar cells. *Org. Lett.* **2012**, *14* (17), 4330−4333.

(6) Liu, B.; Zhu, W.; Zhang, Q.; Wu, W.; Xu, M.; Ning, Z.; Xie, Y.; Tian, H. Conveniently synthesized isophorone dyes for high efficiency dye-sensitized solar cells: tuning photovoltaic performance by structural modification of donor group in donor−π−acceptor system. *Chem. Commun.* **2009**, *13*, 1766−1768.

(7) Kumaresan, D.; Thummel, R. P.; Bura, T.; Ulrich, G.; Ziessel, R. Color Tuning in New Metal-Free Organic Sensitizers (Bodipys) for Dye-Sensitized Solar Cells. *Chem. - Eur. J.* **2009**, *15* (26), 6335−6339.

(8) Yu, G.; Gao, J.; Hummelen, J. C.; Wudl, F.; Heeger, A. J. Polymer Photovoltaic Cells - Enhanced Efficiencies Via a Network of Internal Donor-Acceptor Heterojunctions. *Science* **1995**, *270*, 1789−1791.

(9) Sariciftci, N. S.; Smilowitz, L.; Heeger, A. J.; Wudl, F. Photoinduced Electron-Transfer from a Conducting Polymer to Buckminsterfullerene. *Science* **1992**, *258*, 1474−1476.

(10) Tang, C. W. 2-Layer Organic Photovoltaic Cell. *Appl. Phys. Lett.* **1986**, *48*, 183−185.

(11) Clarke, T. M.; Durrant, J. R. Charge Photogeneration in Organic Solar Cells. *Chem. Rev.* **2010**, *110*, 6736−6767.

(12) Brédas, J. L.; Norton, J. E.; Cornil, J.; Coropceanu, V. Molecular Understanding of Organic Solar Cells: The Challenges. *Acc. Chem. Res.* **2009**, *42*, 1691−1699.

(13) Deibel, C.; Strobel, T.; Dyakonov, V. Role of the Charge Transfer State in Organic Donor-Acceptor Solar Cells. *Adv. Mater.* **2010**, *22*, 4097−4111.
(14) Grancini, G.; Maiuri, M.; Fazzi, D.; Petrozza, A.; Egelhaaf, H. J.; Brida, D.; Cerullo, G.; Lanzani, G. Hot exciton dissociation in polymer solar cells. *Nat. Mater.* **2013**, *12*, 29−33.
(15) Bakulin, A. A.; Rao, A.; Pavelyev, V. G.; van Loosdrecht, P. H. M.; Pshenichnikov, M. S.; Niedzialek, D.; Cornil, J.; Beljonne, D.; Friend, R. H. The Role of Driving Energy and Delocalized States for Charge Separation in Organic Semiconductors. *Science* **2012**, *335*, 1340−1344.
(16) Jailaubekov, A. E.; Willard, A. P.; Tritsch, J. R.; Chan, W. L.; Sai, N.; Gearba, R.; Kaake, L. G.; Williams, K. J.; Leung, K.; Rossky, P. J.; Zhu, X. Y. Hot charge-transfer excitons set the time limit for charge separation at donor/acceptor interfaces in organic photovoltaics. *Nat. Mater.* **2013**, *12*, 66−73.
(17) Vandewal, K.; Albrecht, S.; Hoke, E. T.; Graham, K. R.; Widmer, J.; Douglas, J. D.; Schubert, M.; Mateker, W. R.; Bloking, J. T.; Burkhard, G. F.; Sellinger, A.; Frechet, J. M. J.; Amassian, A.; Riede, M. K.; McGehee, M. D.; Neher, D.; Salleo, A. Efficient charge generation by relaxed charge-transfer states at organic interfaces. *Nat. Mater.* **2014**, *13*, 63−68.
(18) Hwang, I. W.; Soci, C.; Moses, D.; Zhu, Z. G.; Waller, D.; Gaudiana, R.; Brabec, C. J.; Heeger, A. J. Ultrafast electron transfer and decay dynamics in a small band gap bulk heterojunction material. *Adv. Mater.* **2007**, *19*, 2307−2312.
(19) Liu, J.; Chen, S. S.; Qian, D. P.; Gautam, B.; Yang, G. F.; Zhao, J. B.; Bergqvist, J.; Zhang, F. L.; Ma, W.; Ade, H.; Inganäs, O.; Gundogdu, K.; Gao, F.; Yan, H. Fast charge separation in a non-fullerene organic solar cell with a small driving force. *Nat. Energy* **2016**, *1*, 1−7.
(20) Ziółek, M.; Cohen, B.; Yang, X.; Sun, L.; Paulose, M.; Varghese, O. K.; Grimes, C. A.; Douhal, A. Femtosecond to millisecond studies of electron transfer processes in a donor-(pi-spacer)-acceptor series of organic dyes for solar cells interacting with titania nanoparticles and ordered nanotube array films. *Phys. Chem. Chem. Phys.* **2012**, *14* (8), 2816−31.
(21) Kahmann, S.; Gomulya, W.; Loi, M. A.; Mura, A. Donor-acceptor photoexcitation dynamics in organic blends investigated with a high sensitivity pump- probe system. *J. Mater. Chem. C* **2018**, *6* (40), 10822−10828.
(22) Li, C.; Liu, M. Y.; Pschirer, N. G.; Baumgarten, M.; Müllen, K. Polyphenylene-Based Materials for Organic Photovoltaics. *Chem. Rev.* **2010**, *110*, 6817−6855.
(23) Avlasevich, Y.; Li, C.; Müllen, K. Synthesis and applications of core-enlarged perylene dyes. *J. Mater. Chem.* **2010**, *20*, 3814−3826.
(24) Zhu, L. J.; Jiao, C. J.; Xia, D. H.; Wu, J. S. N-Annulated perylene dyes with adjustable photophysical properties. *Tetrahedron Lett.* **2011**, *52*, 6411−6414.
(25) Jiao, C. J.; Huang, K. W.; Guan, Z. P.; Xu, Q. H.; Wu, J. S. N-Annulated Perylene Fused Porphyrins with Enhanced Near-IR Absorption and Emission. *Org. Lett.* **2010**, *12*, 4046−4049.
(26) Li, Y.; Wang, Z. H. Bis-N-Annulated Quaterrylene: An Approach to Processable Graphene Nanoribbons. *Org. Lett.* **2009**, *11*, 1385−1387.
(27) Zeng, Z. B.; Ishida, M.; Zafra, J. L.; Zhu, X. J.; Sung, Y. M.; Bao, N. N.; Webster, R. D.; Lee, B. S.; Li, R. W.; Zeng, W. D.; Li, Y.; Chi, C. Y.; Navarrete, J. T. L.; Ding, J.; Casado, J.; Kim, D.; Wu, J. S. Pushing Extended p-Quinodimethanes to the Limit: Stable Tetracyano-oligo(N-annulated perylene)quinodimethanes with Tunable Ground States. *J. Am. Chem. Soc.* **2013**, *135*, 6363−6371.
(28) Zeng, Z. B.; Lee, S.; Son, M.; Fukuda, K.; Burrezo, P. M.; Zhu, X. J.; Qi, Q. B.; Li, R. W.; Navarrete, J. T. L.; Ding, J.; Casado, J.; Nakano, M.; Kim, D.; Wu, J. S. Push-Pull Type Oligo(N-annulated perylene)quinodimethanes: Chain Length and Solvent-Dependent Ground States and Physical Properties. *J. Am. Chem. Soc.* **2015**, *137*, 8572−8583.
(29) Luo, J.; Xu, M. F.; Li, R. Z.; Huang, K. W.; Jiang, C. Y.; Qi, Q. B.; Zeng, W. D.; Zhang, J.; Chi, C. Y.; Wang, P.; Wu, J. S. N-Annulated Perylene as An Efficient Electron Donor for Porphyrin-Based Dyes: Enhanced Light-Harvesting Ability and High-Efficiency Co(II/III)-Based Dye-Sensitized Solar Cells. *J. Am. Chem. Soc.* **2014**, *136*, 265−272.
(30) Yang, L.; Zheng, Z. W.; Li, Y.; Wu, W. J.; Tian, H.; Wang, Z. H. N-Annulated perylene-based metal-free organic sensitizers for dye-sensitized solar cells. *Chem. Commun.* **2015**, *51*, 4842−4845.
(31) Luo, J.; Wang, X. Z.; Fan, L.; Li, G. Q.; Qi, Q. B.; Huang, K. W.; Tam, T. L. D.; Zhang, J.; Wang, Q.; Wu, J. S. N-Annulated perylene as a donor in cyclopentadithiophene based sensitizers: the effect of the linking mode. *J. Mater. Chem. C* **2016**, *4*, 3709−3714.
(32) Luo, J.; Zhang, J.; Huang, K. W.; Qi, Q. B.; Dong, S. Q.; Zhang, J.; Wang, P.; Wu, J. S. N-Annulated perylene substituted zinc-porphyrins with different linking modes and electron acceptors for dye sensitized solar cells. *J. Mater. Chem. A* **2016**, *4*, 8428−8434.
(33) Yu, F. T.; Cui, S. C.; Li, X.; Peng, Y. Y.; Yu, Y.; Yun, K.; Zhang, S. C.; Li, J.; Liu, J. G.; Hua, J. L. Effect of anchoring groups on N-annulated perylene-based sensitizers for dye-sensitized solar cells and photocatalytic H_2 evolution. *Dyes Pigm.* **2017**, *139*, 7−18.
(34) Chen, H. J.; He, C.; Yu, G.; Zhao, Y.; Huang, J. Y.; Zhu, M. L.; Liu, H. T.; Guo, Y. L.; Li, Y. F.; Liu, Y. Q. Phenanthro[1,10,9,8-cdefg]carbazole-containing copolymer for high performance thin-film transistors and polymer solar cells. *J. Mater. Chem.* **2012**, *22*, 3696−3698.
(35) Qi, Q. B.; Wang, X. Z.; Fan, L.; Zheng, B.; Zeng, W. D.; Luo, J.; Huang, K. W.; Wang, Q.; Wu, J. S. N-Annulated Perylene-Based Push-Pull-Type Sensitizers. *Org. Lett.* **2015**, *17*, 724−727.
(36) Gupta, R. K.; Pathak, S. K.; Pradhan, B.; Shankar Rao, D. S.; Krishna Prasad, S.; Achalkumar, A. S. Self-assembly of luminescent N-annulated perylene tetraesters into fluid columnar phases. *Soft Matter* **2015**, *11* (18), 3629−36.
(37) Yao, Z. Y.; Yan, C. C.; Zhang, M.; Li, R. Z.; Cai, Y. C.; Wang, P. Solar Cells: N-Annulated Perylene as a Coplanar pi-Linker Alternative to Benzene as a Low Energy-Gap, Metal-Free Dye in Sensitized Solar Cells. *Adv. Energy Mater.* **2014**.
(38) Yang, L.; Ren, Y. M.; Yao, Z. Y.; Yan, C. C.; Ma, W. T.; Wang, P. Electron-Acceptor-Dependent Light Absorption and Charge-Transfer Dynamics in N-Annulated Perylene Dye-Sensitized Solar Cells. *J. Phys. Chem. C* **2015**, *119*, 980−988.
(39) Suzuki, K.; Kobayashi, A.; Kaneko, S.; Takehira, K.; Yoshihara, T.; Ishida, H.; Shiina, Y.; Oishi, S.; Tobita, S. Reevaluation of absolute luminescence quantum yields of standard solutions using a spectrometer with an integrating sphere and a back-thinned CCD detector. *Phys. Chem. Chem. Phys.* **2009**, *11* (42), 9850−9860.
(40) Kim, T. W.; Jun, S.; Ha, Y.; Yadav, R. K.; Kumar, A.; Yoo, C. Y.; Oh, I.; Lim, H. K.; Shin, J. W.; Ryoo, R.; Kim, H.; Kim, J.; Baeg, J. O.; Ihee, H. Ultrafast charge transfer coupled with lattice phonons in two-dimensional covalent organic frameworks. *Nat. Commun.* **2019**, *10* (1), 1873.
(41) Frisch, M. J.; Trucks, G. W.; Schlegel, H. B.; Scuseria, G. E.; Robb, M. A.; Cheeseman, J. R.; Scalmani, G.; Barone, V.; Petersson, G. A.; Nakatsuji, H.; et al. *Gaussian 16, Rev. C.01*; Gaussian Inc.: Wallingford, CT, 2016.
(42) Skripnikov, L. *Chemissian 4.43*, A Computer Program to Analyze and Visualize Quantum-chemical Calculations, 2016.
(43) Zhang, Y.; Steyrleuthner, R.; Bredas, J.-L. Charge Delocalization in Oligomers of Poly(2,5-bis(3-alkylthiophene-2-yl)thieno[3,2-b]thiophene) (PBTTT). *J. Phys. Chem. C* **2016**, *120*, 9671−9677.
(44) Halasinski, T. M.; Weisman, J. L.; Ruiterkamp, R.; Lee, T. J.; Salama, F.; Head-Gordon, M. Electronic absorption spectra of neutral perylene ($C_{20}H_{12}$), terrylene ($C_{30}H_{16}$), and quaterrylene ($C_{40}H_{20}$) and their positive and negative ions: Ne matrix-isolation spectroscopy and time-dependent density functional theory calculations. *J. Phys. Chem. A* **2003**, *107* (19), 3660−3669.
(45) Koch, M.; Myahkostupov, M.; Oblinsky, D. G.; Wang, S.; Garakyaraghi, S.; Castellano, F. N.; Scholes, G. D. Charge Localization after Ultrafast Photoexcitation of a Rigid Perylene Perylenediimide Dyad Visualized by Transient Stark Effect. *J. Am. Chem. Soc.* **2017**, *139* (15), 5530−5537.

https://dx.doi.org/10.1021/acs.jpcc.0c06532
J. Phys. Chem. C 2020, 124, 22993−23003

(46) Caspar, J. V.; Meyer, T. J. Application of the Energy-Gap Law to Nonradiative, Excited-State Decay. *J. Phys. Chem.* **1983**, *87*, 952−957.
(47) Bixon, M.; Jortner, J.; Cortes, J.; Heitele, H.; Michelbeyerle, M. E. Energy-Gap Law for Nonradiative and Radiative Charge-Transfer in Isolated and in Solvated Supermolecules. *J. Phys. Chem.* **1994**, *98*, 7289−7299.
(48) Banerji, N.; Angulo, G.; Barabanov, I.; Vauthey, E. Intramolecular charge-transfer dynamics in covalently linked perylene-dimethylaniline and cyanoperylene-dimethylaniline. *J. Phys. Chem. A* **2008**, *112*, 9665−9674.
(49) Sasaki, S.; Drummen, G. P. C.; Konishi, G. Recent advances in twisted intramolecular charge transfer (TICT) fluorescence and related phenomena in materials chemistry. *J. Mater. Chem. C* **2016**, *4*, 2731−2743.
(50) Zhu, H.; Li, M.; Hu, J.; Wang, X.; Jie, J.; Guo, Q.; Chen, C.; Xia, A. Ultrafast Investigation of Intramolecular Charge Transfer and Solvation Dynamics of Tetrahydro[5]-helicene-Based Imide Derivatives. *Sci. Rep.* **2016**, *6*, 24313.
(51) Maffeis, V.; Brisse, R.; Labet, V.; Jousselme, B.; Gustavsson, T. Femtosecond Fluorescence Upconversion Study of a Naphthalimide-Bithiophene-Triphenylamine Push-Pull Dye in Solution. *J. Phys. Chem. A* **2018**, *122*, 5533−5544.
(52) Gustavsson, T.; Coto, P. B.; Serrano-Andrés, L.; Fujiwara, T.; Lim, E. C. Do fluorescence and transient absorption probe the same intramolecular charge transfer state of 4-(dimethylamino)-benzonitrile? *J. Chem. Phys.* **2009**, *131*, 031101.
(53) Rafiq, S.; Yadav, R.; Sen, P. Femtosecond Excited-State Dynamics of 4-Nitrophenyl Pyrrolidinemethanol: Evidence of Twisted Intramolecular Charge Transfer and Intersystem Crossing Involving the Nitro Group. *J. Phys. Chem. A* **2011**, *115*, 8335−8343.
(54) Choi, J.; Ahn, D. S.; Oang, K. Y.; Cho, D. W.; Ihee, H. Charge Transfer-Induced Torsional Dynamics in the Excited State of 2,6-Bis(diphenylamino)anthraquinone. *J. Phys. Chem. C* **2017**, *121*, 24317−24323.
(55) Yanai, T.; Tew, D. P.; Handy, N. C. A new hybrid exchange-correlation functional using the Coulomb-attenuating method (CAM-B3LYP). *Chem. Phys. Lett.* **2004**, *393*, 51−57.
(56) Martin, R. L. Natural transition orbitals. *J. Chem. Phys.* **2003**, *118*, 4775−4777.
(57) Park, M.; Kim, C. H.; Joo, T. Multifaceted ultrafast intramolecular charge transfer dynamics of 4-(dimethylamino)-benzonitrile (DMABN). *J. Phys. Chem. A* **2013**, *117* (2), 370−7.
(58) Banerji, N.; Fürstenberg, A.; Bhosale, S.; Sisson, A. L.; Sakai, N.; Matile, S.; Vauthey, E. Ultrafast photoinduced charge separation in naphthalene diimide based multichromophoric systems in liquid solutions and in a lipid membrane. *J. Phys. Chem. B* **2008**, *112* (30), 8912−8922.
(59) Guo, Y.; Ma, Z.; Niu, X.; Zhang, W.; Tao, M.; Guo, Q.; Wang, Z.; Xia, A. Bridge-Mediated Charge Separation in Isomeric N-Annulated Perylene Diimide Dimers. *J. Am. Chem. Soc.* **2019**, *141* (32), 12789−12796.
(60) Kuang, Z. R.; He, G. Y.; Song, H. W.; Wang, X.; Hu, Z. B.; Sun, H. T.; Wan, Y.; Guo, Q. J.; Xia, A. D. Conformational Relaxation and Thermally Activated Delayed Fluorescence in Anthraquinone-Based Intramolecular Charge-Transfer Compound. *J. Phys. Chem. C* **2018**, *122*, 3727−3737.
(61) Karunakaran, V.; Das, S. Direct Observation of Cascade of Photoinduced Ultrafast Intramolecular Charge Transfer Dynamics in Diphenyl Acetylene Derivatives: Via Solvation and Intramolecular Relaxation. *J. Phys. Chem. B* **2016**, *120* (28), 7016−23.
(62) Yoshihara, T.; Druzhinin, S. I.; Zachariasse, K. A. Fast intramolecular charge transfer with a planar rigidized electron donor/acceptor molecule. *J. Am. Chem. Soc.* **2004**, *126* (27), 8535−9.
(63) Maroncelli, M.; Fleming, G. R. Comparison of time-resolved fluorescence Stokes shift measurements to a molecular theory of solvation dynamics. *J. Chem. Phys.* **1988**, *89* (2), 875−881.
(64) Horng, M. L.; Gardecki, J. A.; Papazyan, A.; Maroncelli, M. Subpicosecond Measurements of Polar Solvation Dynamics - Coumarin-153 Revisited. *J. Phys. Chem.* **1995**, *99*, 17311−17337.
(65) Reynolds, L.; Gardecki, J. A.; Frankland, S. J. V.; Horng, M. L.; Maroncelli, M. Dipole solvation in nondipolar solvents: Experimental studies of reorganization energies and solvation dynamics. *J. Phys. Chem.* **1996**, *100*, 10337−10354.
(66) Jimenez, R.; Fleming, G. R.; Kumar, P. V.; Maroncelli, M. Femtosecond Solvation Dynamics of Water. *Nature* **1994**, *369*, 471−473.
(67) Fee, R. S.; Maroncelli, M. Estimating the Time-Zero Spectrum in Time-Resolved Emission Measurements of Solvation Dynamics. *Chem. Phys.* **1994**, *183*, 235−247.
(68) Kim, J.; Kim, D. E.; Joo, T. Excited-State Dynamics of Thioflavin T: Planar Stable Intermediate Revealed by Nuclear Wave Packet Spectroscopies. *J. Phys. Chem. A* **2018**, *122*, 1283−1290.
(69) Chi, X. C.; Wang, Y. H.; Gao, Y.; Sui, N.; Zhang, L. Q.; Wang, W. Y.; Lu, R.; Ji, W. Y.; Yang, Y. Q.; Zhang, H. Z. Acceptor number-dependent ultrafast photo-physical properties of push-pull chromophores using time-resolved methods. *Chem. Phys. Lett.* **2018**, *698*, 127−131.
(70) Reid, P. J.; Barbara, P. F. Dynamic Solvent Effect on Betaine-30 Electron-Transfer Kinetics in Alcohols. *J. Phys. Chem.* **1995**, *99*, 3554−3565.
(71) Kovalenko, S. A.; Eilers-König, N.; Senyushkina, T. A.; Ernsting, N. P. Charge transfer and solvation of betaine-30 in polar solvents - A femtosecond broadband transient absorption study. *J. Phys. Chem. A* **2001**, *105*, 4834−4843.
(72) Rafiq, S.; Scholes, G. D. Is back-electron transfer process in Betaine-30 coherent? *Chem. Phys. Lett.* **2017**, *683*, 500−506.
(73) Dereka, B.; Svechkarev, D.; Rosspeintner, A.; Tromayer, M.; Liska, R.; Mohs, A. M.; Vauthey, E. Direct Observation of a Photochemical Alkyne-Allene Reaction and of a Twisted and Rehybridized Intramolecular Charge-Transfer State in a Donor-Acceptor Dyad. *J. Am. Chem. Soc.* **2017**, *139* (46), 16885−16893.
(74) Ghosh, R.; Nandi, A.; Palit, D. K. Solvent sensitive intramolecular charge transfer dynamics in the excited states of 4-N, N-dimethylamino-4′-nitrobiphenyl. *Phys. Chem. Chem. Phys.* **2016**, *18* (11), 7661−7671.
(75) Weil, T.; Vosch, T.; Hofkens, J.; Peneva, K.; Müllen, K. The Rylene Colorant Family-Tailored Nanoemitters for Photonics Research and Applications. *Angew. Chem., Int. Ed.* **2010**, *49* (48), 9068−9093.

https://dx.doi.org/10.1021/acs.jpcc.0c06532
J. Phys. Chem. C 2020, 124, 22993−23003